nature nanotechnology

ARTICLES

https://doi.org/10.1038/s41565-019-0367-4

Unravelling inherent electrocatalysis of mixed-conducting oxide activated by metal nanoparticle for fuel cell electrodes

Yoonseok Choi[1,5], Seung Keun Cha[1,2,5], Hyunwoo Ha[3,5], Siwon Lee[1], Hyeon Kook Seo[1,4], Jeong Yong Lee[1,4], Hyun You Kim[3*], Sang Ouk Kim[1,2*] and WooChul Jung[1*]

Highly active metal nanoparticles are desired to serve in high-temperature electrocatalysis, for example, in solid oxide electrochemical cells. Unfortunately, the low thermal stability of nanosized particles and the sophisticated interface requirement for electrode structures to support concurrent ionic and electronic transport make it hard to identify the exact catalytic role of nanoparticles embedded within complex electrode architectures. Here we present an accurate analysis of the reactivity of oxide electrodes boosted by metal nanoparticles, where all particles participate in the reaction. Monodisperse particles (Pt, Pd, Au and Co), 10 nm in size and stable at high temperature (more than 600 °C), are uniformly distributed onto mixed-conducting oxide electrodes as a model electrochemical cell via self-assembled nanopatterning. We identify how the metal catalysts activate hydrogen electrooxidation on the ceria-based electrode surface and quantify how rapidly the reaction rate increases with proper choice of metal. These results suggest an ideal electrode design for high-temperature electrochemical applications.

Solid oxide electrochemical cells (SOCs) offer an eco-friendly means of energy storage and conversion, where energy can be either stored in the form of a chemical fuel (electrolysis mode) or converted into electricity at a remarkably high level of efficiency (fuel-cell mode). A long-standing bottleneck in the development of practically meaningful SOC technology is the high cost associated with cell fabrication and operation, largely because of the high operation temperature, typically in the range of 800–900 °C (refs. [1,2]). Lowering the operation temperature of SOCs below 600 °C may extend the choice of materials to less expensive options (that is, stainless steel as an interconnect material) and allow the realization of long lifetimes along with minimal thermomechanical degradation and less burden for device sealing[3]. Unfortunately, the electrochemical resistances of essential cell components such as electrodes increase rapidly at low temperatures due to the high activation energy required for the electrocatalytic reaction. Accordingly, designing a catalytic structure with a low activation barrier is crucial for the eventual success of SOC technology[4,5].

Metal nanoparticles have become a key component in high-performance heterogeneous catalysts, primarily serving as a catalytic activator. Recent experimental and theoretical findings suggest that optimization of the chemical nature at the metal/support interfaces is essential for performance improvement[6,7]. Meanwhile, previous efforts towards the utilization of metal nanoparticles in SOCs have suffered because of the poor thermal stability of the nanoparticles[8]. Nanosized metal particles readily coalesce and grow at high operating temperatures, leading to severe catalytic activity losses[9,10]. This inherent problem can be partially addressed through the use of thermally stable inorganic support materials such as mesoporous silica[11–13] or gas-permeable oxide shells[14,15]. These support materials are commonly dielectrics, but metal nanoparticles for SOCs must simultaneously come into contact with percolating ionic and electronic transport pathways to allow effective electrochemical reactions[5,16].

Recently, there have been a few reports of the successful incorporation of metal nanoparticles (with diameters of 10 nm or less) onto SOC electrodes, where the nanoparticles are stabilized on a scaffold of mixed ionic and electronic conducting oxides with highly porous morphology. The use of the mixed conductive oxide as an electrode allows the metal particles dispersed on the electrode to actively participate in the electrochemical reaction, and the porous electrode structure effectively blocks agglomeration of the particles. Substantially improved electrode activity for hydrogen electrooxidation and decent sintering resistance of Pt, Pd, Ni and Co-decorated porous columnar $Sm_{0.2}Ce_{0.8}O_{1.9}$ films have been demonstrated[17], and it has been shown that Ni nanoparticles are formed by the selective diffusion of Ni along the grain boundary of $Sm_{0.2}Ce_{0.8}O_{1.9}$ films and the subsequent reduction, which exhibited excellent H_2 electrooxidation activity and thermal stability[18]. Others have reported that submonolayer $Pd@CeO_2$ core–shell nanocomposite catalysts improve the performance of yttria-stabilized zirconia (YSZ)/$La_{0.8}Sr_{0.2}Cr_{0.5}Mn_{0.5}O_3$ electrodes[19]. The performance of Ag-doped $Sr_{0.95}Nb_{0.1}Co_{0.9}O_3$ electrodes has been enhanced by extruding Ag nanoparticles from the oxide lattice via partial reduction, while enhanced activity was analogously achieved with a Co- or Ni-doped $PrBaMn_2O_{5+\delta}$ electrode[20–22]. These findings clearly imply the potential of metal nanoparticles as an optimizer of SOC electrodes, particularly for lower-temperature operation (≤600 °C). Nonetheless, the underlying mechanism for the enhancement of the catalytic performance and the exact role of nanoparticles in the electrochemical reaction remain unclear. Given the morphological complexity of typical porous metal/oxide composite electrodes along with the

[1]Department of Materials Science and Engineering, KAIST, Daejeon, Republic of Korea. [2]National Creative Research Initiative Center for Multi-Dimensional Directed Nanoscale Assembly, KAIST, Daejeon, Republic of Korea. [3]Department of Materials Science and Engineering, Chungnam National University, Daejeon, Republic of Korea. [4]Center for Nanomaterials and Chemical Reactions, Institute for Basic Science (IBS), Daejeon, Republic of Korea. [5]These authors contributed equally: Y. Choi, S. K. Cha, H. Ha. *e-mail: kimhy@cnu.ac.kr; sangouk.kim@kaist.ac.kr; wcjung@kaist.ac.kr

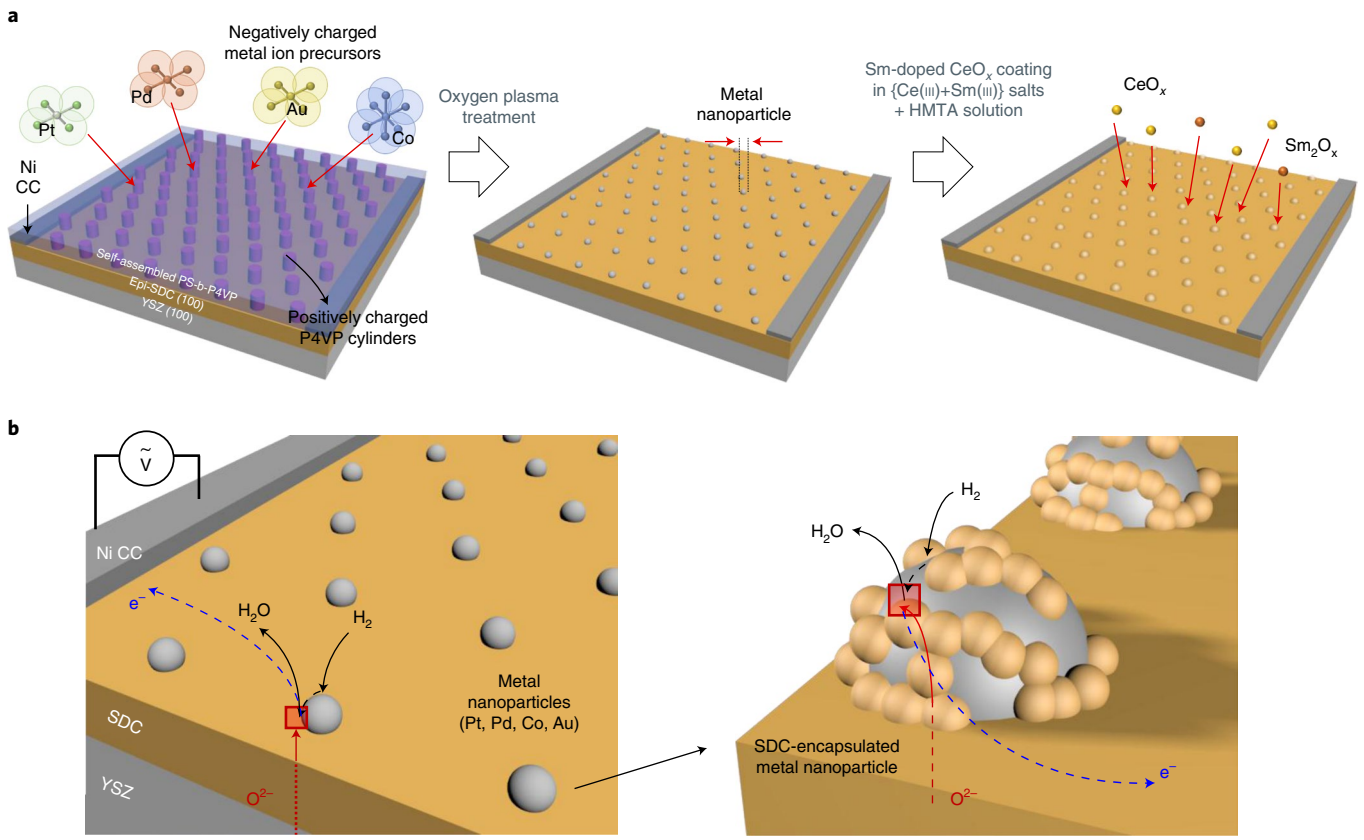

Fig. 1 | A metal-decorated model thin-film electrode. a, Schematic flowchart of the fabrication process for the model symmetric electrochemical cell used in this study. The dispersion of the monoarray of metal nanoparticles follows the nanopattern of the self-assembled block copolymer (block copolymer lithography). **b**, Schematic illustration of hydrogen electrooxidation on a SDC surface decorated with monodisperse bare metal nanoparticles (left) and SDC-encapsulated metal nanoparticles (right). Oxygen ions pass vertically through the SDC thin film from the electrolyte, and electrons are collected horizontally through the SDC thin film into Ni current collectors (CC). Epi, epitaxial; HMTA, hexamethylenetetramine; PS-b-P4VP, polystyrene-block-poly(4-vinylpyridine).

uneven distribution of polydisperse nanoparticles[23,24], a quantitative analysis of the intrinsic contribution of metal nanoparticles to the overall catalytic performance of metal/oxide electrodes is a formidable challenge[7,25]. Thus, it has never been possible to answer the following fundamental questions. "How much exactly can a single metal nanoparticle contribute to the high-temperature electrocatalysis of oxide electrodes?" "How does the electrocatalysis change with the composition of the metal particles, perfectly differentiated from structural complexity?" "What is the ideal electrode performance that a given amount of metal catalysts can achieve if all metal nanoparticles are fully used for electrochemical reactions without aggregation at high temperatures?"

To address these issues, we present an ideal model electrode system with well-defined uniform catalyst geometries and intimate three-phase interfaces with ionic and electronic conductors for a precise analysis of the nanoparticle-catalysed electrochemical reaction. Figure 1a illustrates the fabrication process and structure of our symmetric electrochemical cell. Epitaxial films (thickness of 1 μm) of $Sm_{0.2}Ce_{0.8}O_{1.9-\delta}$ (Sm-doped ceria, SDC) were deposited as the working electrode on both sides of the YSZ single-crystal electrolyte substrate by pulsed laser deposition (PLD), after which Ni strip arrays (20 μm width and 20 μm spacing) were patterned on the surface of the SDC films as counter-electrodes (Supplementary Fig. 1). SDC was selected as the electrode material because of its high electron and oxygen ion conductivities and excellent inherent activity towards hydrogen electrooxidation—the target model reaction in this study[26–28]. Well-ordered arrays of monodisperse metal nanoparticles were prepared on the SDC electrodes via block copolymer (BCP) self-assembled nanotemplates[29,30]. Finally, the metal nanoparticles were encapsulated with gas-permeable thin layers of SDC to avoid coalescence. It is noteworthy that this judicious design of the electrode enables idealized three-phase interface at each nanoparticle for barrier-free ionic and electronic transport through the bottom SDC layer and nearby metal array, respectively, as well as an exact measurement of the catalytic geometry of the well-defined monodisperse nanoparticle array (Fig. 1b).

Physical and chemical characterization of model electrodes

Figure 2a–d presents scanning electron microscopy (SEM) images of electrode surfaces with ordered metal nanoparticles before and after the SDC coating process. Each hexagonal packed particle array exhibits remarkably narrow distributions of particle diameter, inter-particle spacing and areal number density (10.1 ± 1.4 nm, 30.7 ± 0.9 nm and $(1.1 \pm 0.3) \times 10^{11}$ cm^{-2}, respectively) (Supplementary Fig. 2). All particles are evenly covered by an SDC layer approximately 4 nm thick via precipitation and a dry process using metal-nitride precursors (Fig. 2a–d, insets). Cross-sectional transmission electron microscopy (TEM) images (Fig. 2e,f) indicate that the Pt particles on the SDC electrode are encapsulated by a thin SDC layer, with further evidence provided by fast Fourier transform (FFT) results and X-ray photoelectron spectroscopy (XPS) depth-profiling (Supplementary Fig. 3). The SDC coating layer uniformly covers both the Pt nanoparticles and the SDC electrode, ensuring good interfacial contact for the electron

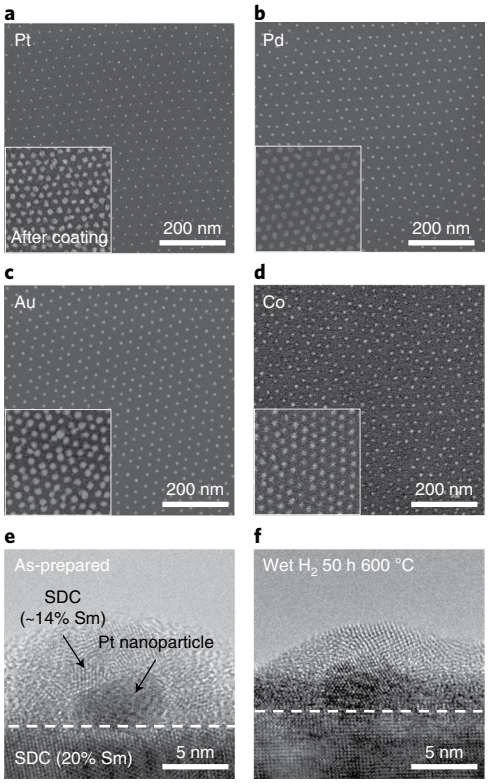

Fig. 2 | Microscopy images of metal nanoparticles on thin-film ceria. **a–d**, SEM images of monodisperse metal nanoparticles; Pt (8.3 ± 1.8 nm) (**a**), Pd (10.2 ± 1.7 nm) (**b**), Au (10.2 ± 1.2 nm) (**c**) and Co (11.8 ± 2.6 nm) (**d**). Inset, SEM images of metal nanoparticles encapsulated in a thin SDC layer with a thickness of 4.0 ± 0.2 nm on the same scale as the main image (for histograms for each particle diameter see Supplementary Fig. 2). **e**,**f**, TEM images of as-prepared SDC-encapsulated Pt nanoparticles: as deposited (**e**) and after 50 h of impedance measurements at 600 °C (**f**).

and ion transport pathways simultaneously required for electrochemical reactions. Reactant gases can also reach the metal catalyst through the mesoscale pores formed during the transformation of hydrated cerium oxy-hydroxide into CeO_2 (refs. [8,31]). Indeed, the SDC-coated metal nanoparticles show reliable thermal stability without any agglomeration or penetration of Pt into the SDC coating layers, even at 600 °C and 50 h of impedance measurement (Supplementary Figs. 3d and 4a). Thermal annealing at 700 °C for 10 h under ambient air or CO atmosphere does not cause clustering (Supplementary Fig. 4b,c). These results show that the model electrode platform proposed in this study can be widely applied to various reactions, such as CO electrooxidation or oxygen reduction reactions (ORRs). It should be noted that bare Pt particles, unlike other metals, show excellent sintering resistance up to 500 °C on the ceria surface[32], allowing high-temperature impedance analysis without the need for an SDC coating, as discussed in the following (Supplementary Fig. 4d,e).

Electrochemical measurement of model electrodes

The electrochemical reactivity of the structurally well-defined metal-coated oxide thin-film electrodes was analysed with regard to H_2 electrooxidation by a.c. impedance spectroscopy at 400–650 °C in a wet hydrogen atmosphere. With or without nanoparticles, the zero-bias impedance response of each sample, plotted in Nyquist form, commonly consists of an offset resistance and only a single semicircle at a lower frequency (Fig. 3a). The offset resistance is readily attributed to the sum of the YSZ bulk and the Ni sheet resistance and is omitted from the present spectra to reduce the degree of complexity. Thus, the low-frequency impedance arc reflects the characteristics of the electrochemical reaction occurring on the SDC electrode surface[27,33]. The most significant key feature is the nanoparticle-dependent response of the electrode resistance, displayed as the diameter of the arc, which decreases remarkably with nanoparticles. For instance, bare Pt nanoparticles reduce the resistance of the SDC electrode down to 1/12 or to 1/37 when an additional SDC layer surrounds them. The corresponding activation energy is also reduced from 0.89 eV to 0.57–0.60 eV by the incorporation of Pt nanoparticles, as presented in the Arrhenius plot in Fig. 3b. These observations provide clear evidence that the measured impedance reflects the surface electrochemical response of the SDC electrode, not bulk ionic or electronic conduction[33], and that the Pt nanoparticles accelerate the rate of H_2 oxidation on the SDC surface. It is particularly noteworthy that the electrode impedance decreases linearly with the total number of nanoparticles dispersed on the electrode surface. Figure 3c shows that as the surface area of the SDC exposed to hydrogen gas quadruples and thus the number of Pt nanoparticles decorated on the SDC also quadruples (Supplementary Fig. 1e,f), the electrode resistance decreases by a factor of exactly four. Furthermore, we also doubled the areal number density of Pt nanoparticles by replacing the BCPs with a different molecular mass, which in turn reduces the electrode resistance by half (Fig. 3d). These results ensure that all nanoparticles dispersed on the electrode surface fully participate in the surface electrochemical reaction, which is essential to quantify the contribution of metal particles to the electrochemical reactivity.

The structural regularity of nanopatterned metal nanoparticles allows geometric quantification of possible reaction sites, such as exposed Pt areas or Pt–SDC interfaces. The impedance results for SDC electrodes with Pt particles of different sizes and spacings, as shown in Fig. 3d, are good examples. In this case, the electrode resistance values obtained from the two samples are surprisingly consistent when normalized by the Pt–SDC interface length, not by the exposed Pt surface areas (Supplementary Table 1). This suggests that the Pt–SDC interface is the dominant active site for the H_2 electrooxidation reaction. It is further supported by the observation that the SDC-coated Pt nanoparticles exhibit a lower electrode resistance than bare Pt nanoparticles, despite the reduced bare surface area in the presence of the coating layer (Fig. 3b). Indeed, both Pt–SDC and coated-Pt–SDC share the same activation energy but differ only in the electrode resistance. The resistance also slightly decrease as the coating layer becomes thicker (up to 11 nm) and reaches an almost constant value (Supplementary Fig. 5a). Considering that the coating layers tend to limit the exposed Pt sites, all these results can be attributed to the enlarged density of the Pt–SDC interface with the SDC coating (Supplementary Fig. 5a), as similarly reported in CeO_2-encapsulated Pt catalysts[8,34]. We thus present experimental evidence directly showing the electrochemical activity of the Pt–ceria interface for H_2 electrooxidation reaction kinetics at elevated temperature. Although the exact nature of the systems and operative mechanisms may be different, this observation agrees well with the previous experimental and theoretical findings for the synergetic interaction at the Pt–ceria interface[6,35–37], as further discussed in our density functional theory (DFT) results ('Theoretical interpretation' section).

Intrinsic electrocatalysis of metal nanoparticles

Given the identified reaction site and the quantified total length of the metal–ceria interface, our measurement enables us to estimate the inherent electrochemical activities of Pt catalysts. Table 1 summarizes the electrode conductance value quantified with respect to the interface length of the Pt–SDC, a key reaction site ($5.18 \times 10^{-7}\,\Omega^{-1}\,cm^{-1}$ at 500 °C). More significantly, we could obtain the turnover frequency (TOF) of the nanoparticles, a representative

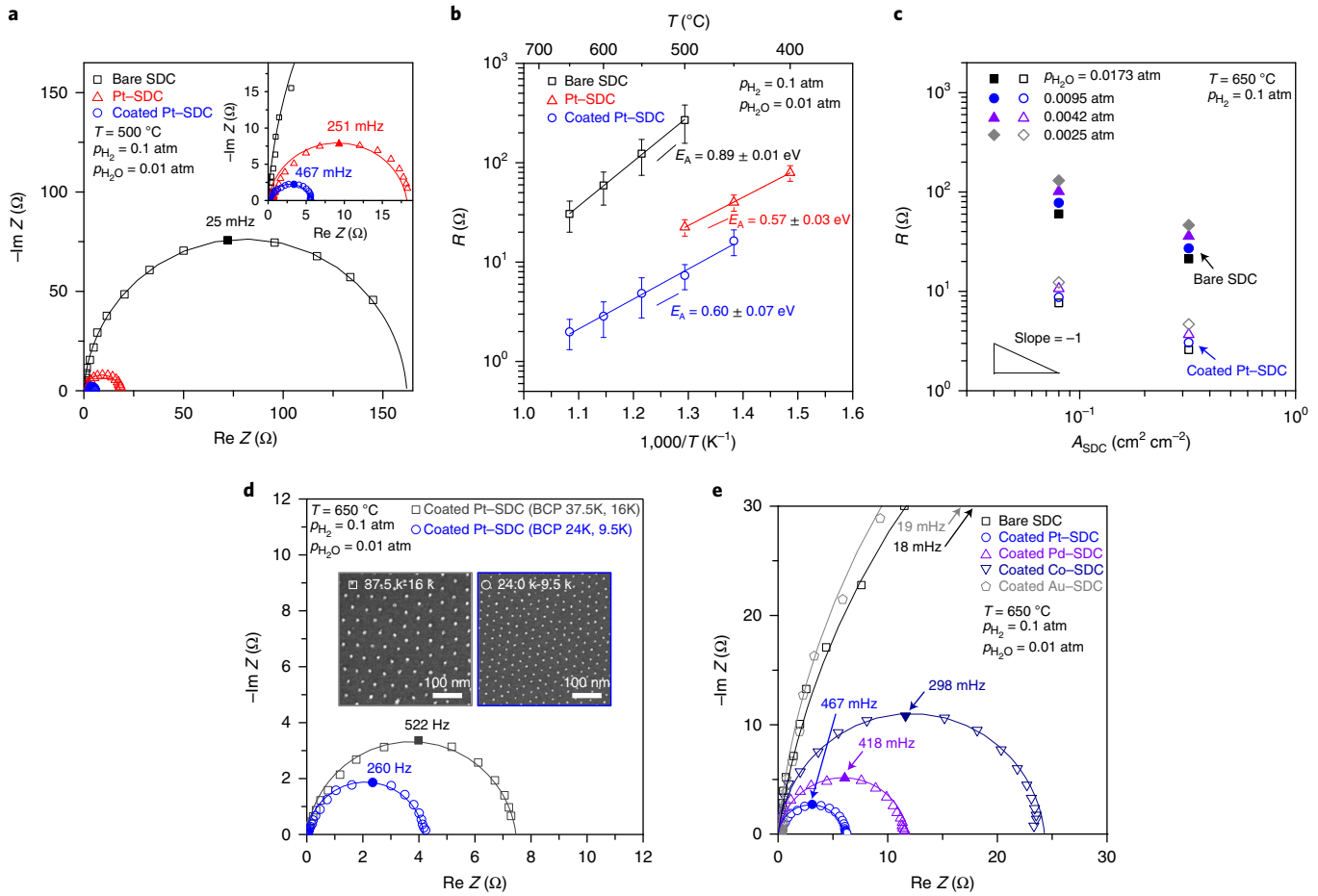

Fig. 3 | Electrochemical analysis of metal-decorated SDC electrodes. a, Typical impedance (Z) spectra of patterned Ni|SDC|YSZ(100)|SDC|patterned Ni symmetric cells with or without Pt catalysts measured at 500 °C, p_{H_2} = 0.1 atm and p_{H_2O} = 0.01 atm: bare SDC; SDC with Pt nanoparticles (Pt-SDC); SDC with SDC-encapsulated Pt nanoparticles (coated Pt-SDC). Filled data point indicates maximum point of the impedance. **b**, Arrhenius plot of the electrode resistance (R) of bare SDC, Pt-SDC and coated Pt-SDC measured at p_{H_2} = 0.1 atm and p_{H_2O} = 0.01 atm. **c**, Double logarithmic plot of electrode resistance R of bare SDC (filled symbols) and coated Pt-SDC (open symbols) cells versus SDC area (A_{SDC}), p_{H_2} = 0.1 atm at T = 650 °C. A_{SDC} represents the projected area of the SDC thin-film electrodes. **d**, Impedance response varying with metal nanoparticle dispersion, measured at 650 °C, p_{H_2} = 0.1 atm and p_{H_2O} = 0.01 atm. Inset, SEM images of Pt nanoparticles (before SDC coating) obtained by using different molecular mass of BCPs: 37.5K, 16K indicates M_n = 37.5 kg mol^{-1} for PS and 16 kg mol^{-1} for P4VP (left); 24.0K, 9.5K indicates M_n = 24.0 kg mol^{-1} for PS and 9.5 kg mol^{-1} for P4VP (right). **e**, Comparison of the impedance spectra of patterned Ni|SDC|YSZ(100)|SDC|patterned Ni symmetric cells with four different metal catalysts measured at 600 °C, p_{H_2} = 0.1 atm and p_{H_2O} = 0.01 atm. Error bars in **b** account for the standard deviation from average resistance values obtained from two to four samples.

intrinsic catalytic property for them (see Supplementary Discussion). The calculated TOF of the Pt nanoparticles was found to be 1.13×10^3 s^{-1} at 500 °C, which is nearly four orders of magnitude greater than the value for the low-temperature CO oxidation of nanocatalysts of a similar size and composition ($(7.61 \pm 0.97) \times 10^{-1}$ s^{-1} at 80 °C) (see Methods). This confirms the excellent reactivity of metal nanoparticles in high-temperature electrochemical reactions based on our first quantitative measurements, with a high level of accuracy.

In contrast, with consistent size and distribution of the four different metals, the electrode resistance obtained with the four different metal nanoparticles directly reflects their inherent catalytic activity, differentiated from any geometrical effect. As can be seen in Fig. 3e, under the indicated conditions (10% H_2/1% H_2O and 600 °C), the incorporation of Pt, Pd and Co nanoparticles reduces the resistance of a bare SDC electrode down to 1/21, 1/11 and 1/6, respectively, whereas there is a negligible impact by Au nanoparticles. This shows that, among the tested materials, the best performance is observed with Pt nanoparticles, Pd nanoparticles have better activity than Co nanoparticles, while Au nanoparticles are considered to be inactive catalysts for H_2 electrooxidation. For Pt nanoparticles, the obtained area-specific resistance (ASR) of 2.4 ± 0.7 Ω cm^2 at 500 °C is remarkably low given the flat surface geometry of the model electrode and with a very low amount of Pt nanoparticles (with a loading of only 360 ng cm^{-2}). This value is even smaller than that for porous nanocolumnar SDC electrodes, whose specific surface area is 20.6 m^2 g^{-1}, approximately 120 times larger than the SDC surface used in this work[38]. We suggest that such low ASR levels for the SDC-coated metal nanoparticles indicate the ideally achievable electrode performance with a given amount of metal catalyst at high temperature. More specifically, Table 2 shows the electrode conductance values normalized by the number and mass of metal nanoparticles as well as the interface-site density between metal and ceria in a humidified H_2 atmosphere. For instance, a single Pt particle (10 nm in size) improves the electrode conductance by 1.08×10^{-11} Ω^{-1} at 600 °C, and is 2.3, 4.2 and 30 times more reactive than Pd, Co and Au, respectively.

Theoretical interpretation

To verify the experimental observations, we carried out detailed DFT calculations of the H_2 oxidation on pristine and metal-coated

Table 1 | Intrinsic reactivity of the Pt-decorated SDC electrode

Temperature (°C)	Electrode conductance[a] ($10^{-7}\,\Omega^{-1}\,cm^{-1}$)	TOF per unit length of Pt-SDC ($10^{2}\,s^{-1}$)[b]
500	5.18	11.3
450	2.62	5.70
400	1.79	3.89

[a]Electrode conductance of Pt–SDC normalized with respect to the unit length of the Pt–SDC interfaces. The Pt–SDC length was estimated by assuming a hemispherical shape for the Pt particle and using the corresponding diameter values shown in Supplementary Fig. 2. [b]TOF of Pt–SDC toward the H_2 electrooxidation reaction, obtained under a wet H_2 atmosphere (p_{H_2} = 0.1 atm, p_{H_2O} = 0.01 atm) at T = 400–500 °C (see Supplementary Discussion).

Table 2 | Normalized electrode conductance of the metal-decorated SDC electrodes

	Electrode conductance[a] normalized by	
	Number of particles ($10^{-12}\,\Omega^{-1}$ per particle)	Loading amount ($10^{-1}\,\Omega^{-1}\,\mu g^{-1}$)
Pt	10.8	33.7
Pd	4.70	14.1
Co	2.60	6.83
Au	≤0.36	≤0.66

[a]Electrode conductance ($1/R$) of four different coated metal nanoparticles (Pt, Pd, Co and Au), obtained under a wet H_2 atmosphere (p_{H_2} = 0.1 atm, p_{H_2O} = 0.01 atm) at T = 600 °C, normalized with respect to the number of particles. [b]The loading amount was estimated by assuming a hemispherical shape and using the corresponding diameter values shown in Supplementary Fig. 2 (Pt, 359 ng; Pd, 374 ng; Co, 426 ng; Au, 601 ng).

SDC (100) surfaces (Fig. 4). First, unlike a pristine or vacated ceria (100) surface (Supplementary Fig. 6a), SDC was found to bind H_2 dissociatively with an average binding energy (E_{bind}) of −1.60 eV (Fig. 4a). Because the Sm dopants donate fewer electrons to the adjacent oxygen ions than the lattice Ce ions, they weaken the Ce–O ionic bonding and increase the hydrogen affinity of the weakly negatively charged oxygen ions. The reduced oxygen vacancy formation energy of SDC (100) compared to CeO_2 (refs. [39,40]) ($E_{vac} \approx -0.29$–0.26 eV) confirms the modified electronic structure of CeO_2 following Sm doping (Supplementary Fig. 7). Considering that H_2 activation in this work occurs under a high H_2 partial pressure, the SDC surface would be readily saturated with H atoms, as evidenced by recent X-ray photoelectron spectroscopy observations[41,42]. These adsorbed H atoms donate electrons to the reduced oxygen ions of SDC, strengthening the Ce–O ionic interaction of hydrogenated SDC. As a result, H_2O desorption and oxygen vacancy formation requires a relatively high energy (E_{des}) of 1.42 eV, which suggests that the H_2O desorption becomes the rate-determining step (RDS) for H_2 oxidation by SDC.

Pt nanoparticles supported on SDC further modify the hydrogen chemistry of the SDC while donating electrons to it (Fig. 4b and Supplementary Fig. 10a). Noticeably, a more dramatic electronic change occurs following H_2 binding on Pt–SDC. The Pt nanoparticles of Pt–SDC (Fig. 4b and Supplementary Fig. 10b) also dissociatively binds H_2 (ref. [43]). The dissociated H atoms can subsequently be transferred to the SDC surface. The rate of H transfer estimated by harmonic–transition state theory ($4.2 \times 10^9\,s^{-1}$ at 773 K) predicts that the facile hydrogen spillover occurs from the Pt nanoparticles to SDC (Supplementary Fig. 11)[44]. This calculation can also be supported by the relatively weak dependence of the electrode resistance on $p_{H_2}{}^n$, with a power exponent (n) between 0.25 and 0.29, regardless of the presence of Pt nanoparticles (Supplementary Fig. 5b). The hydrogen spillover from the Pt nanoparticle to the adjacent O ion at the Pt–SDC interface was found to facilitate an electron transfer from H to O. Consequently, following saturation of the surface oxygen ions of SDC with 17H atoms, all Ce^{4+} surface ions are reduced to Ce^{3+} and the Pt nanoparticle becomes electronically neutral (Supplementary Fig. 10c). The average binding energy of 17H atoms on the lattice oxygen ions of Pt–SDC (average E_{bind} = −1.34 eV) is slightly lower than the value calculated for SDC (average E_{bind} = −1.60 eV).

A remarkable difference was found in the E_{des} values of water from the H-saturated Pt–SDC and SDC. The average E_{des} of Pt–SDC was 0.08 eV, even less than 10% of that of bare SDC, particularly when H_2O is desorbed at the interface between Pt and SDC. Given that the desorption of H_2O is the RDS, our calculation confirms that metal-catalysed water desorption supports the experimentally observed acceleration in the overall H_2 oxidation kinetics, particularly at the region near the metal–ceria interface. These results are also strongly supported by the consistency between the E_{des} values and the experimentally measured catalytic performances of the tested metal nanoparticles (Supplementary Fig. 12a–d). The average E_{des} value of water from Pd–SDC (E_{des} = 0.81 eV) lies between the values for Pt–SDC and bare SDC. In contrast, the average E_{des} of water from Au–SDC (E_{des} = 1.37 eV) is as high as that of bare SDC. Here, to identify the underlying mechanism, we note that water desorption accompanies an electron transfer from Pt–SDC to the water molecule, where a considerable percentage of these electrons are supplied from the Pt nanoparticles. The presence of Pt nanoparticles, an additional electron reservoir, is highly beneficial for facile water generation, and they enhance the electronic versatility of the system. As shown in Fig. 4c (Supplementary Fig. 12e–h), the DOS for H-saturated Pt–SDC illustrates that Pt nanoparticles generate extra electron states near the Fermi level. Given that the Pd nanoparticle also generates extra electron states near the Fermi level, it also promotes H_2 oxidation. The DOS of Au–SDC shows no extra electron state near the Fermi level of SDC, and its morphologies near the Fermi level are nearly identical to that of SDC. Our results provide evidence that electronic interaction between metal nanoparticles and ceria electrodes can control the overall electrocatalytic performance of the nanoparticle–oxide system[36,37].

Recognition of the exact role of metal nanoparticles for high-temperature electrocatalysis offers guidance for a design rule for creating SOC electrodes with exceptional performance. Surprisingly, a minimum amount of metal nanoparticles can greatly enhance the electrode performance if all particles are uniformly dispersed and stably interfaced with fuel, electron and ion transport pathways. It is also important to take advantage of the catalytic synergy in strong interactions between metal nanoparticles and supports, even during high-temperature electrochemical reactions, such as those at the Pt–SDC electrode. Therefore, it is indispensable to select a suitable metal/oxide combination for electrode materials and to develop a method for uniform metal particle dispersion on the oxide surface while suppressing particle agglomeration. Taken together, these efforts should allow the realization of high-temperature electrodes with unparalleled electrocatalytic activities.

Conclusions

In summary, an ideal model platform has been introduced for analysis of the high-temperature electrocatalysis of an oxide electrode surface promoted by metal nanoparticles, utilizing an advanced nanoscale patterning method. Our unprecedented quantitative measurements confirm that the metal–ceria interface is electrochemically active for the H_2 oxidation reaction. We identify that the metal nanoparticles activate water desorption at the metal–ceria interface, which is an RDS, by donating extra electrons to accelerate the overall reaction kinetics, suggesting that it is key to take advantage of the catalytic synergy during metal–support interactions,

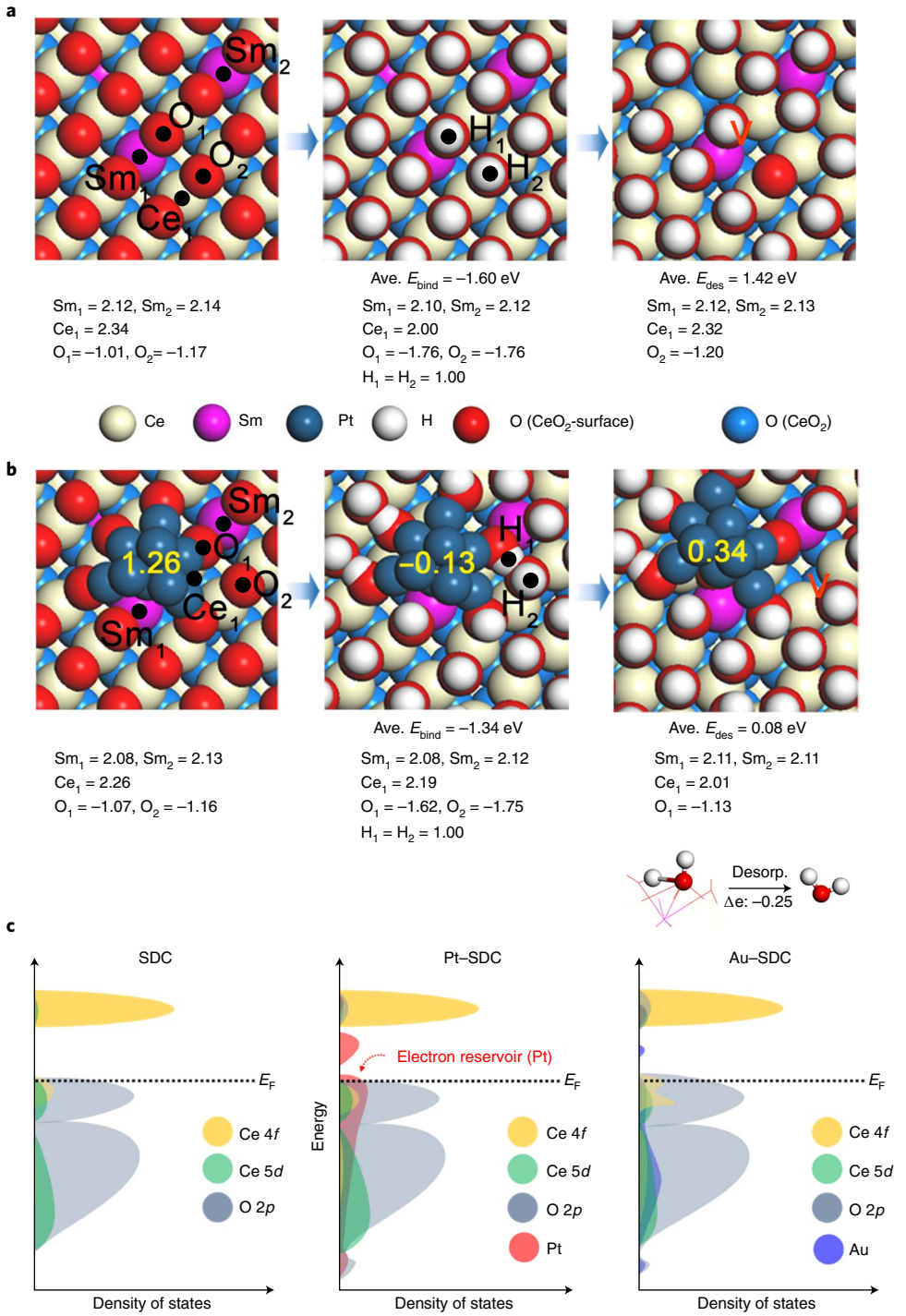

Fig. 4 | Reaction pathway of H_2 electrooxidation on bare SDC and metal-decorated SDC electrodes. a, H_2 electrooxidation pathway on bare SDC with the energetics of H_2 adsorption and H_2O production. **b**, H_2 electrooxidation pathway on the Pt-coated SDC with the energetics and electron redistribution for each step. The Bader charges of selected ions are given below each panel. The total Bader charge of the Pt nanoparticle is presented in yellow. The Pt nanoparticle of Pt–SDC binds and transfers H atoms to the interfacial oxygen ions of SDC (hydrogen spillover). Note that the Pt nanoparticle supplies extra electrons to SDC following H_2O desorption from the Pt–SDC interface (see Supplementary Information for details). **c**, Density of states (DOS) obtained from DFT calculations for H-saturated bare SDC, Pt–SDC and Au–SDC (see Supplementary Information for the H-saturated Pd–SDC and detailed DOS results). The Pt nanoparticle of Pt–SDC generates extra electron states at the Fermi level, a process that is beneficial for facile H_2O production. Ave., average; Δe, change in number of electrons.

even during high-temperature electrochemical reactions, such as those at the Pt–SDC electrode. Additionally, a smart selection of suitable metal/oxide combinations for electrode materials can be achieved through this measurement platform. Overall, this work proposes a reliable design rule for creating catalytic structures for high-temperature electrocatalytic reactions over a broad range of solid-state devices, such as fuel cells, electrolysers, sensors and photoelectrochemical cells.

Online content

Any methods, additional references, Nature Research reporting summaries, source data, statements of data availability and associated accession codes are available at https://doi.org/10.1038/s41565-019-0367-4.

Received: 20 August 2018; Accepted: 4 January 2019;
Published online: 18 February 2019

References

1. Shao, Z. P. & Haile, S. M. A high-performance cathode for the next generation of solid-oxide fuel cells. *Nature* **431**, 170–173 (2004).
2. Wachsman, E. D. & Lee, K. T. Lowering the temperature of solid oxide fuel cells. *Science* **334**, 935–939 (2011).
3. Seo, H. G., Choi, Y. & Jung, W. Exceptionally enhanced electrode activity of $(Pr,Ce)O_{2-\delta}$-based cathodes for thin-film solid oxide fuel cells. https://doi.org/10.1002/aenm.201703647 (2018).
4. Gao, Z. et al. A perspective on low-temperature solid oxide fuel cells. *Energy Environ. Sci.* **9**, 1602–1644 (2016).
5. Irvine, J. T. S. et al. Evolution of the electrochemical interface in high-temperature fuel cells and electrolysers. *Nat. Energy* **1**, 15014 (2016).
6. Vayssilov, G. N. et al. Support nanostructure boosts oxygen transfer to catalytically active platinum nanoparticles. *Nat. Mater.* **10**, 310–315 (2011).
7. Cargnello, M. et al. Control of metal nanocrystal size reveals metal–support interface role for ceria catalysts. *Science* **341**, 771–773 (2013).
8. Lee, S., Seo, J. & Jung, W. Sintering-resistant $Pt@CeO_2$ nanoparticles for high-temperature oxidation catalysis. *Nanoscale* **8**, 10219–10228 (2016).
9. Cao, A., Lu, R. & Veser, G. Stabilizing metal nanoparticles for heterogeneous catalysis. *Phys. Chem. Chem. Phys.* **12**, 13499–13510 (2010).
10. Cao, A. & Veser, G. Exceptional high-temperature stability through distillation-like self-stabilization in bimetallic nanoparticles. *Nat. Mater.* **9**, 75–81 (2010).
11. Gabaldon, J. P., Bore, M. & Datye, A. K. Mesoporous silica supports for improved thermal stability in supported Au catalysts. *Top Catal.* **44**, 253–262 (2007).
12. Joo, S. H. et al. Thermally stable Pt/mesoporous silica core–shell nanocatalysts for high-temperature reactions. *Nat. Mater.* **8**, 126–131 (2009).
13. Prieto, G. et al. Towards stable catalysts by controlling collective properties of supported metal nanoparticles. *Nat. Mater.* **12**, 34–39 (2013).
14. Arnal, P. M., Comotti, M. & Schuth, F. High-temperature-stable catalysts by hollow sphere encapsulation. *Angew. Chem. Int. Ed.* **45**, 8224–8227 (2006).
15. Lu, J. L. et al. Coking- and sintering-resistant palladium catalysts achieved through atomic layer deposition. *Science* **335**, 1205–1208 (2012).
16. Uchida, H., Suzuki, H. & Watanabe, M. High-performance electrode for medium-temperature solid oxide fuel cells—effects of composition and microstructures on performance of ceria-based anodes. *J. Electrochem. Soc.* **145**, 615–620 (1998).
17. Jung, W., Gu, K. L., Choi, Y. & Haile, S. M. Robust nanostructures with exceptionally high electrochemical reaction activity for high temperature fuel cell electrodes. *Energy Environ. Sci.* **7**, 1685–1692 (2014).
18. Kwak, N. W. et al. In situ synthesis of supported metal nanocatalysts through heterogeneous doping. *Nat. Commun.* **9**, 4829 (2018).
19. Adijanto, L. et al. Synthesis and stability of $Pd@CeO_2$ core–shell catalyst films in solid oxide fuel cell anodes. *ACS Catal.* **3**, 1801–1809 (2013).
20. Zhu, Y. L. et al. Promotion of oxygen reduction by exsolved silver nanoparticles on a perovskite scaffold for low-temperature solid oxide duel xells. *Nano Lett.* **16**, 512–518 (2016).
21. Kwon, O. et al. Exsolution trends and co-segregation aspects of self-grown catalyst nanoparticles in perovskites. *Nat. Commun.* **8**, 15967 (2017).
22. Kwon, O. et al. Self-assembled alloy nanoparticles in a layered double perovskite as a fuel oxidation catalyst for solid oxide fuel cells. *J. Mater. Chem. A* **6**, 15947–15953 (2018).
23. Jiang, S. P. Nanoscale and nano-structured electrodes of solid oxide fuel cells by infiltration: advances and challenges. *Int. J. Hydrogen Energy* **37**, 449–470 (2012).
24. Connor, P. A. et al. Tailoring SOFC electrode microstructures for improved performance. *Adv. Energy Mater.* **8**, 1800120 (2018).
25. Myung, J. H., Neagu, D., Miller, D. N. & Irvine, J. T. S. Switching on electrocatalytic activity in solid oxide cells. *Nature* **537**, 528–531 (2016).
26. Lai, W. & Haile, S. M. Impedance spectroscopy as a tool for chemical and electrochemical analysis of mixed conductors: a case study of ceria. *J. Am. Ceram. Soc.* **88**, 2979–2997 (2005).
27. Chueh, W. C., Hao, Y., Jung, W. & Haile, S. M. High electrochemical activity of the oxide phase in model ceria–Pt and ceria–Ni composite anodes. *Nat. Mater.* **11**, 155–161 (2012).
28. Choi, Y., Brown, E. C., Haile, S. M. & Jung, W. Electrochemically modified, robust solid oxide fuel cell anode for direct-hydrocarbon utilization. *Nano Energy* **23**, 161–171 (2016).
29. Mun, J. H. et al. Monodisperse pattern nanoalloying for synergistic intermetallic catalysis. *Nano Lett.* **13**, 5720–5726 (2013).
30. Cha, S. K. et al. Au–Ag core–shell nanoparticle array by block copolymer lithography for synergistic broadband plasmonic properties. *ACS Nano* **9**, 5536–5543 (2015).
31. Polezhaeva, O. S., Yaroshinskaya, N. V. & Ivanov, V. K. Formation mechanism of nanocrystalline ceria in aqueous solutions of cerium(III) nitrate and hexamethylenetetramine. *Inorg. Mater.* **44**, 51–57 (2008).
32. Shinjoh, H. Noble metal sintering suppression technology in three-way catalyst: automotive three-way catalysts with the noble metal sintering suppression technology based on the support anchoring effect. *Catal. Surv. Asia* **13**, 184–190 (2009).
33. Chen, C., Chen, D., Chueh, W. C. & Ciucci, F. Modeling the impedance response of mixed-conducting thin film electrodes. *Phys. Chem. Chem. Phys.* **16**, 11573–11583 (2014).
34. Wang, X., Liu, D. P., Song, S. Y. & Zhang, H. J. $Pt@CeO_2$ multicore@shell self-assembled nanospheres: clean synthesis, structure optimization, and catalytic applications. *J. Am. Chem. Soc.* **135**, 15864–15872 (2013).
35. Bruix, A. et al. A new type of strong metal–support interaction and the production of H_2 through the transformation of water on $Pt/CeO_2(111)$ and $Pt/CeO_x/TiO_2(110)$ catalysts. *J. Am. Chem. Soc.* **134**, 8968–8974 (2012).
36. Campbell, C. T. Catalyst–support interactions: electronic perturbations. *Nat. Chem.* **4**, 597–598 (2012).
37. Lykhach, Y. et al. Counting electrons on supported nanoparticles. *Nat. Mater.* **15**, 284–288 (2016).
38. Jung, W. et al. High electrode activity of nanostructured, columnar ceria films for solid oxide fuel cells. *Energy Environ. Sci.* **5**, 8682–8689 (2012).
39. Kim, H. Y. & Henkelman, G. CO oxidation at the interface of Au nanoclusters and the stepped-CeO_2 (111) surface by the Mars–van Krevelen mechanism. *J. Phys. Chem. Lett.* **4**, 216–221 (2013).
40. Ha, H., Yoon, S., An, K. & Kim, H. Y. Catalytic CO oxidation over Au nanoparticles supported on CeO_2 nanocrystals: effect of the $Au–CeO_2$ interface. *ACS Catal.* **8**, 11491–11501 (2018).
41. Zhang, C. J. et al. Mechanistic studies of water electrolysis and hydrogen electro-oxidation on high temperature ceria-based solid oxide electrochemical cells. *J. Am. Chem. Soc.* **135**, 11572–11579 (2013).
42. Feng, Z. A. et al. Fast vacancy-mediated oxygen ion incorporation across the ceria–gas electrochemical interface. *Nat. Commun.* **5**, 4374 (2014).
43. Lykhach, Y. et al. Oxide-based nanomaterials for fuel cell catalysis: the interplay between supported single Pt atoms and particles. *Catal. Sci. Technol.* **7**, 4315–4345 (2017).
44. Karim, W. et al. Catalyst support effects on hydrogen spillover. *Nature* **541**, 68–71 (2017).

Acknowledgements

Y.C., S.L. and W.J. were supported financially by the Nano·Material Technology Development Program (NRF-2017M3A7B4049507), the Global Frontier R&D Program (2011-0031569) and the Basic Research Program (2014R1A4A1003712) through the National Research Foundation of Korea (NRF) funded by the Ministry of Science, ICT and Future Planning. S.K.C. and S.O.K. were supported financially by the National Creative Research Initiative (CRI) Center for Multi-Dimensional Directed Nanoscale Assembly (2015R1A3A2033061) funded by NRF. H.H. and H.Y.K. acknowledge financial support from National Research Foundation of Korea (NRF) grants funded by the Korea government (MSIP) (2017R1A2B4009829 and 2017R1A4A1015360). H.K.S. and J.Y.L. were supported financially by the Institute for Basic Science (IBS-R004-D1). This research used resources of the Center for Functional Nanomaterials, which is a US DOE Office of Science Facility, and the Scientific Data and Computing Center, a part of the Computational Science Initiative at Brookhaven National Laboratory (contract no. DE-SC0012704).

Author contributions

Y.C., S.L. and W.J. conceived the idea for this study. Y.C. prepared the electrode cells and collected the electrocatalytic data. S.K.C. synthesized metal nanoparticles using BCP. H.H. performed DFT calculations. S.L. performed the CO oxidation test. H.K.S. and J.Y.L. performed TEM characterization. W.J., S.O.K. and H.Y.K. supervised the project and wrote the manuscript. All authors commented on the data and the manuscript.

Competing interests

The authors declare no competing interests.

Additional information

Supplementary information is available for this paper at https://doi.org/10.1038/s41565-019-0367-4.

Reprints and permissions information is available at www.nature.com/reprints.

Correspondence and requests for materials should be addressed to H.Y.K., S.O.K. or W.J.

Publisher's note: Springer Nature remains neutral with regard to jurisdictional claims in published maps and institutional affiliations.

© The Author(s), under exclusive licence to Springer Nature Limited 2019

Methods

A symmetric electrochemical cell configuration (current collector|electrode|electrolyte|electrode|current collector) was used in this study. Ni pattern strips were fabricated as a current collector by photolithography on thin-film electrodes of SDC, which in turn were obtained by PLD on a YSZ electrolyte substrate. The fabrication processes described in the following sections were repeated in the same way on both sides.

Fabrication of Ni-patterned SDC films. Epitaxial SDC thin films (1 μm thick) were grown on a (100) single-crystal YSZ substrate (8 mol%, 10×10×0.5 mm, MTI) by PLD (KrF 248 nm excimer laser, Lambda Physik 205, 300 mJ, 20 Hz) with an oxide target made using a solid-state method (Fuelcellmaterials, 99.999%). The deposition temperature was 600 °C and the working pressure of the chamber (filled with oxygen gas, 99.999%) was 10 mTorr. Sacrificial YSZ layers were inserted between the substrate and the heater stage to avoid contamination.

Patterned Ni films were obtained via a photolithographic liftoff process. A positive photoresist (AZ5214) was spin-coated onto SDC films at 3,000 r.p.m. and baked at 115 °C for 1 min. The samples were exposed to ultraviolet light for 10 s while in contact with a photomask after alignment by a contact aligner (MDA-8000B, MIDAS). The samples were then immersed in developer for 50 s to obtain the photoresist patterns, followed by rinsing in deionized (DI) water, drying and baking at 120 °C for 2 min. Before Ni deposition, oxygen plasma treatment (200 W for 5 min) was conducted to clean the sample surfaces. Ni films (300 nm thick, 99.99% target purity) were deposited by d.c. magnetron sputtering with a d.c. power of 100 W, working pressure of 10 mTorr Ar and deposition rate of ~1 nm s^{-1}. The final Ni patterns were obtained by immersing the samples in acetone at room temperature under mild ultrasonication.

Synthesis of SDC-encapsulated metal nanoparticle arrays. Asymmetric polystyrene-block-poly(4-vinylpyridine) (PS-b-P4VP, M_n = 24 kg mol^{-1} for PS and 9.5 kg mol^{-1} for P4VP, Polymer Source) BCP was dissolved in a toluene and tetrahydrofuran (THF) mixture (3:1 weight ratio; 0.5 wt% solution). The PS-b-P4VP BCP solution was spin-coated onto the Ni-patterned SDC films at a suitable speed. As-cast BCP thin films were solvent-annealed in chambers saturated with the toluene/THF mixture (1:4 volume ratio) to induce a perpendicularly aligned cylindrical morphology. The annealed BCP samples were immersed in acidic aqueous solutions containing four different metal precursors (K_2PtCl_4, Na_2PdCl_4, $K_3Co(CN)_6$ and $HAuCl_4$) to load metal ions into the P4VP nanocylinders. Details of the conditions used to yield a similar size for all metal nanoclusters are provided in Supplementary Table 2. After rinsing in DI water, the polymer on the samples was perfectly etched by oxygen plasma. The metal nanoparticle arrays were then immersed in an aqueous solution of $Ce(NO_3)_3$ (1 mM) and $Sm(NO_3)_3$ (0.07 mM) at 70 °C. Hexamethylenetetramine (10 mM) was added into the solution, to oxidize the Ce and Sm precursors onto metal nanoparticle seeds. The thickness of the SDC coating layer was controlled by the immersion time. The SDC-encapsulated metal nanoparticle arrays were rinsed in DI water, dried with N_2 gas and annealed at 250 °C for 2 h to cluster and stabilize the particles.

Physical characterizations. The physical properties of the symmetrical cells were characterized by SEM (Hitachi S-4800) and high-resolution X-ray diffraction (X'Pert-PRO MRD) using K_α(Cu) radiation (45 kV, 40 mA). TEM analysis (Titan ETEM G2, 300 kV) was also performed to examine the microstructure of the SDC-encapsulated metal nanoparticles. Information about the distribution and size of the bare or encapsulated metal nanoparticles was also obtained by image-processing software (Inspector 2.1). The chemical composition of the nanocomposite catalysts was analysed by XPS (K-alpha).

Electrochemical analyses. The electrocatalytic performances of the symmetric cells with or without SDC-encapsulated metal nanoparticles were investigated with a.c. impedance spectroscopy (VSP-300, Biologic) under a wet hydrogen atmosphere in the temperature range 450–700 °C. A perturbation amplitude of 10 mV at zero bias was used with a measurement frequency range of 0.01 Hz–1 MHz. The cells were placed inside an alumina tube in contact with a pseudo-four-configuration probe to minimize the inductance effects from the wiring. The mixture gases (H_2–H_2O–N_2) were flowed into the tube with a total flow rate of 100 s.c.c.m. (gas velocity of 19.7 cm min^{-1}), controlled by digital mass flow controllers. The humidity of the gases was controlled by passing them through a DI water bubbler immersed in an isothermal bath, fixed at 10 °C, and monitored using a humidity sensor (Rotronic Hygroflex).

CO oxidation test of Pt nanoparticles. For a quantitative comparison of the TOF values, a CO oxidation test was performed on Pt nanoparticles supported on CeO_2 powders. An aqueous solution of tetradecyltrimethylammonium bromide (400 mM, 12.5 ml) and K_2PtCl_4 (10 mM, 5 ml) was mixed with DI water (29.5 ml) and stirred at 300 r.p.m. at room temperature for 10 min in a 100 ml round-bottomed flask. The solution was then heated to 50 °C in an oil bath under continuous stirring for 10 min. An ice-cooled aqueous solution of $NaBH_4$ (500 mM, 3 ml) was added by stabbing the septum with a syringe. The hydrogen gases were then released through a needle. The reacted mixture was maintained at 50 °C for 15 h under magnetic stirring. The resulting brown solution was centrifuged at 3,000 r.p.m. for 30 min to remove the larger Pt nanoparticles. The supernatant solution was separated and centrifuged again at 12,000 r.p.m. for 15 min, twice. The precipitates were collected and redispersed in 5 ml of DI water for further use. The Pt nanoparticle solution (1 wt%, verified by inductively coupled plasma–optical emission spectrometry) was added to a dispersion of ceria in 40 ml basic aqueous solution (pH ≈ 11). Ceria was obtained by calcination of $Ce(NO_3)_3$ in air at 450 °C for 20 h. The mixture was then left stirring for 1 h for complete adsorption. The precipitates were dried at 95 °C in an oven overnight and calcined at 350 °C for 5 h in a box furnace with a ramping rate of 3 °C min^{-1}.

The catalytic activities for CO oxidation were measured in a fixed-bed quartz flow microreactor with an internal diameter of 4 mm. We used 50 mg catalysts mixed with 100 mg quartz sands and loaded them between two plugs of quartz wools to prevent displacement of the catalysts. The reaction gases consisted of 1 vol% CO, 4 vol% O_2 and 95 vol% Ar and were fed at 50 ml min^{-1}, corresponding to a weight hourly space velocity of 60,000 ml g^{-1} h^{-1}. The reactant and product gases were monitored in real time with a quadrupole mass spectrometer (Pfeiffer Vacuum GSD320) connected to the reactor outlet. The CO signal was corrected for the contribution from the cracking fragment of CO_2 using the mass concentration determination mode.

DFT calculations. To find the most stable position of the Sm dopants in ceria, we used a narrow 2×2×6 supercell with six triple-ceria layers. Supplementary Fig. 7 shows the preferred locations of Sm single ion and pairs distributed over the ceria (100) supercell (Supplementary Fig. 7a,b). Based on the results of this pre-DFT calculation, all three Sm ions were located at the surface and the subsurface layer of a 3×3×3 supercell, which is equivalent to an 8.33 at% Sm concentration (Supplementary Figs. 7c and 8). The bottom ceria triple layer was fixed for all calculations to ensure structural robustness. The metal nanoparticles (Pt, Pd and Au) composed of nine atoms were later deposited on the 3×3×3 SDC substrate. The Sm dopants strengthened the metal–ceria interaction. Because the Sm dopants are slightly reduced compared to the conventional Ce^{4+} ions of ceria, the oxygen ions of SDC are capable of binding more strongly the supporting metal nanoparticles (Supplementary Figs. 7c and 9). For H_2 oxidation calculations we consistently saturated the exposed surface oxygen ions of the metal nanoparticles–SDC with total 17H atoms (corresponding to H/O = 1).

We performed generalized gradient approximation-level spin-polarized DFT calculations using a plane-wave basis with the VASP code[45] and PBE functional[46]. To appropriately treat the Ce *f*-orbitals, DFT+U[47] with U_{eff} = 5 eV (refs. [39,40]) was used for Ce ions. No U correction value was assigned for Sm dopants, for which core *f*-electrons are well-localized to Sm ions[48]. The interaction between the ionic core and the valence electrons was described by the projector augmented wave method[49]. Valence electron wavefunctions were expanded in a plane-wave basis up to an energy cutoff of 400 eV. A 2×2×1 *k*-points grid sampling of the Brillouin zone was applied for all initial geometry optimizations with a 3×3 supercell. Later, the Brillouin zone was sampled at the Γ-point for subsequent calculations. A finer 3×3×1 *k*-points grid sampling was applied for a 2×2 supercell. A 6×6×1 *k*-points grid sampling was applied for DOS calculations. The convergence criteria for the electronic structure and atomic geometry were 10^{-4} eV and 0.03 eV $Å^{-1}$, respectively. We used a Gaussian smearing function with a finite temperature width of 0.05 eV to improve the convergence of states near the Fermi level. The location and energy of transition states were calculated with the climbing-image nudged elastic band method[50].

Data availability

The data that support the findings of this study are available from the corresponding author upon reasonable request.

References

45. Kresse, G. & Furthmuller, J. Efficiency of ab-initio total energy calculations for metals and semiconductors using a plane-wave basis set. *Comput. Mater. Sci.* **6**, 15–50 (1996).
46. Perdew, J. P., Burke, K. & Ernzerhof, M. Generalized gradient approximation made simple. *Phys. Rev. Lett.* **77**, 3865–3868 (1996).
47. Dudarev, S. L. et al. Electron-energy-loss spectra and the structural stability of nickel oxide: an LSDA+U study. *Phys. Rev. B* **57**, 1505–1509 (1998).
48. Ismail, A., Giorgi, J. B. & Woo, T. K. On the atomistic interactions that direct ion conductivity and defect segregation in the bulk and surface of samarium-doped ceria: a genetic algorithm study. *J. Phys. Chem. C* **116**, 704–713 (2012).
49. Blochl, P. E. Projector augmented-wave method. *Phys. Rev. B* **50**, 17953–17979 (1994).
50. Henkelman, G. & Jónsson, H. Improved tangent estimate in the nudged elastic band method for finding minimum energy paths and saddle points. *J. Chem. Phys.* **113**, 9978–9985 (2000).